

XRISM view of a stellar flare: High-resolution Fe K spectra of HR 1099, an RS CVn-type star

Miki KURIHARA^{1,2,*}, Masahiro TSUJIMOTO^{1,2}, Michael LOEWENSTEIN³, Yoshitomo MAEDA², Marc AUDARD⁴, Ehud BEHAR⁵, Megan E. ECKART⁶, Adam FOSTER⁷, Liyi GU⁸, Matteo GUAINAZZI⁹, Kenji HAMAGUCHI^{10,3,11}, Natalie HELL⁶, Shun INOUE¹², Yukiko ISHIHARA¹³, Satoru KATSUDA¹⁴, Caroline A. KILBOURNE³, Maurice A. LEUTENEGGER³, Eric D. MILLER¹⁵, Nagisa NAGASHIMA¹³, Frederick Scott PORTER³, Makoto SAWADA¹⁶, Yohko TSUBOI¹³, Vinay L. KASHYAP⁷ and David H. BROOKS^{17,18,2}

¹Department of Astronomy, Graduate School of Science, The University of Tokyo, Bunkyo-ku, Tokyo 113-0033, Japan

²Japan Aerospace Exploration Agency, Institute of Space and Astronautical Science, Chuo-ku, Sagamihara, Kanagawa 252-5210, Japan

³NASA / Goddard Space Flight Center, Greenbelt, MD 20771, USA

⁴Department of Astronomy, University of Geneva, Versoix CH-1290, Switzerland

⁵Department of Physics, Technion, Technion City, Haifa 3200003, Israel

⁶Lawrence Livermore National Laboratory, Livermore, CA 94550, USA

⁷Center for Astrophysics, Harvard-Smithsonian, Cambridge, MA 02138, USA

⁸SRON Netherlands Institute for Space Research, Leiden, The Netherlands

⁹European Space Agency, European Space Research and Technology Centre, Noordwijk, The Netherlands

¹⁰Center for Space Science and Technology, University of Maryland, Baltimore County, Baltimore, MD 21250, USA

¹¹Center for Research and Exploration in Space Science and Technology (CRESST) II, NASA / Goddard Space Flight Center, Greenbelt, MD 20771, USA

¹²Department of Physics, Kyoto University, Sakyo-ku, Kyoto, Kyoto 606-8502, Japan

¹³Department of Physics, Chuo University, Bunkyo-ku, Tokyo 112-8551, Japan

¹⁴Department of Physics, Saitama University, Sakura-ku, Saitama, Saitama 338-8570, Japan

¹⁵Kavli Institute for Astrophysics and Space Research, Massachusetts Institute of Technology, Cambridge, MA 02139, USA

¹⁶Department of Physics, Rikkyo University, Toshima-ku, Tokyo 171-8501, Japan

¹⁷Department of Physics & Astronomy, George Mason University, 4400 University Drive, Fairfax, VA 22030, USA

¹⁸University College London, Mullard Space Science Laboratory, Dorking, Surrey, RH5 6NT, UK

* E-mail: kurihara@ac.jaxa.jp, miki39kurihara@g.ecc.u-tokyo.ac.jp

ORCID: 0000-0002-3133-9053, 0000-0002-9184-5556, 0000-0002-1661-4029, 0000-0002-9099-5755, 0000-0003-4721-034X, 0000-0001-9735-4873, 0000-0003-3894-5889, 0000-0003-3462-8886, 0000-0001-9911-7038, 0000-0002-1094-3147, 0000-0001-7515-2779, 0000-0003-3057-1536, 0000-0003-3085-304X, 0000-0002-1104-7205, 0000-0001-9464-4103, 0000-0002-3331-7595, 0000-0002-3031-2326, 0000-0002-6374-1119, 0000-0003-2008-6887, 0000-0001-9943-0024, 0000-0002-3869-7996, 0000-0002-2189-9313

Abstract

A high-resolution X-ray spectroscopic observation was made of the RS CVn-type binary star HR 1099 using the Resolve instrument onboard XRISM for its calibration purposes. During the \sim 400 ks telescope time covering 1.5 binary orbit, a flare lasting for \sim 100 ks was observed with a released X-ray radiation energy of \sim 10³⁴ erg, making it the first stellar flare ever observed with an X-ray microcalorimeter spectrometer. The flare peak count rate is 6.4 times higher than that in quiescence and is distinguished clearly in time thanks to the long telescope time. Many emission lines were detected in the 1.7–10 keV range both in the flare and quiescent phases. Using the high spectral resolution of Resolve in the Fe K band (6.5–7.0 keV), we resolved the inner-shell lines of Fe XIX–XXIV as well as the outer-shell lines of Fe XXV–XXVI. These lines have peaks in the contribution functions at different temperatures over a wide range, allowing us to construct the differential emission measure (DEM) distribution over the electron temperature of 1–10 keV (roughly 10–100 MK) based only on Fe lines, thus without an assumption of the elemental abundance. The reconstructed DEM has a bimodal distribution, and only the hotter component increased during the flare. The elemental abundance was derived based on the DEM distribution thus constructed. A significant abundance increase was observed during the flare for Ca and Fe, which are some of the elements with the lowest first ionization potential among those analyzed, but not for Si, S, and Ar. This behavior is seen in some giant solar flares and the present result is a clear example in stellar flares.

Keywords: atomic processes, stars: coronae, stars: individual (HR 1099), techniques: spectroscopic, X-rays: stars

1 Introduction

Flares on stars are among the most energetic manifestations of magnetic activity and continue to be intensively studied (e.g., Benz

& Güdel 2010; Kowalski 2024). The standard paradigm of eruptive flares suggests that magnetic reconnection impulsively releases the energy stored in stellar coronae (Priest & Forbes 2002; Shibata & Magara 2011), producing optically thin plasma at temperatures of ~ 0.1 –10 keV that emits both thermal and nonthermal radiation in X-rays. Key properties of coronal plasmas include their thermal structure and chemical composition, as these directly relate to the heating and cooling processes. The physics is considered to be the same with solar flares but observations of magnetically active stars have revealed phenomena not typically seen in the Sun, such as more energetic flares (e.g., Tsuboi et al. 2016) and the inverse first ionization potential (FIP) effect (see Laming 2009, 2015 for reviews).

Since the first discovery of abundance differences between the solar photosphere and corona by Pottasch (1963), studies of the FIP effect have expanded to distant stars (Testa 2010 for a review). The FIP effect refers to the systematic enrichment of low-FIP elements ($\lesssim 10$ eV) or the depletion of high-FIP elements in stellar coronae relative to their photospheric abundances, while the inverse FIP (i-FIP) effect denotes the opposite trend. Although the physical origin remains debated, these behaviors are thought to be related to the coronal heating mechanism itself. Comparative analyses across stellar samples indicate that the strength and sign of the FIP bias depend on activity level (Telleschi et al. 2005; Seli et al. 2022), and this has been extensively studied using X-ray grating spectrometers (e.g., Audard et al. 2003; Nordon & Behar 2008). The target of this study, the RS CVn-type binary HR 1099, is a representative system that served as the first-light target of XMM-Newton (Audard et al. 2001) and is well known to exhibit the i-FIP effect (Brinkman et al. 2001; Drake et al. 2001; Nordon & Behar 2008; Seli et al. 2022).

In this paper, we present the results of a week-long Resolve calibration observation of HR 1099. A stellar flare was captured for the first time with an X-ray microcalorimeter spectrometer. Using this data set, we perform the differential emission measure (DEM) analysis for both the flaring and quiescent phases using the Fe XIX–XXVI K-shell lines, based on which we investigate the changes of the chemical abundance between the two phases.

The outline of this paper is as follows. In § 2, we first describe the method of using the Fe XIX–XXVI K-shell lines ratios for plasma diagnostics. In § 3, we describe the target (§ 3.1), the observation (§ 3.2), and the data reduction (§ 3.3). Some technical details are given to explain the context of this calibration observation made in unusual instrumental configurations and data processing specific to the data. In § 4, we present the Resolve light curve and spectra (§ 4.1), followed by the results of the spectral modeling in the broadband (§ 4.2) and the Fe K complexes (§ 4.3). In § 5, we present two results; the DEM distribution (§ 5.1) and the chemical abundance (§ 5.2), and compare the present data with some previous results. In § 6, we conclude with major findings of this study.

2 Method

In distant stars, neither spatially resolved imaging nor in-situ measurements are possible. Spectroscopy therefore provides the primary means to diagnose the thermal structure and chemical composition of coronal plasma. The thermal structure is commonly characterized by DEM distributions, which represent the emission measure of plasma at each temperature bin integrated over the stellar disk. DEMs for solar and stellar coronae have been con-

structed from emission lines in EUV and X-ray spectra. Several inversion techniques for DEM reconstruction have been developed for the Sun (e.g., Del Zanna & Mason 2018 for a review). Emission line features originate from bound-bound transitions of various elements in different charge states that are affected by thermal structure. A key point here is to use emission lines from ions of a single element across a wide range of ionization states, providing broad temperature coverage and decoupling the degeneracy between DEM shape and elemental abundances.

In stellar X-ray studies, this strategy became feasible with the advent of the grating spectrometers onboard the Chandra (Weisskopf et al. 2000) and XMM-Newton (Jansen et al. 2001) X-ray observatories. In practice, Fe is the only element that can be used for this purpose. Using the Reflection Grating Spectrometer (RGS; Den Herder et al. 2001), Brinkman et al. (2001) used a series of Fe XVII–XXIV L-shell lines at ~ 1 keV. Using the High Energy Transmission Grating (HETG; Canizares et al. 2005), Nordon & Behar (2008) used the Fe XVII–XXIV L-shell lines as well as the Fe XXV K-shell line at 6.7 keV. However, systematic uncertainties remain in the use of this Fe XXV K-shell line in grating missions as unresolved contributions from the lower charged Fe K-shell lines persist. Also, the Fe XXVI lines should be added to constrain the hottest end of the DEM distribution.

In this regard, the use of Fe K-shell lines in the 6.4–7.0 keV range is particularly advantageous. This energy range contains outer-shell transition lines of Fe XXVI and XXV as well as inner-shell transition lines of Fe XXIV and lower charge states, which have become possible with the advent of the microcalorimeter spectrometer. The Resolve instrument (Kelley et al. submitted; Ishisaki et al. 2022) onboard the X-ray Imaging and Spectroscopy Mission (XRISM; Tashiro et al. 2020) provides high-resolution spectra ($R \equiv E/\Delta E \sim 1300$ at the Fe K band) along with broad energy coverage from 1.7 to 12.0 keV. The Fe K-shell lines from different charge states can be resolved for constructing the DEM distribution over a wide temperature range. In addition, strong K-shell lines of Si through Ni can be used to derive the elemental abundance.

Figure 1 illustrates the concept of this diagnostic. The temperature range, in which representative lines of different charge states are dominant, are shown. For example, the Fe XXVI Ly α lines ($2p^2P \rightarrow 1s^2S$) at 7.0 keV are formed primarily by the direct excitation in H-like Fe ion at the ground state followed by radiative decay. Therefore, the contribution function of the line reflects H-like Fe population function dominant over a temperature range of $10^{0.4}$ – $10^{1.1}$ keV. Other lines cover different ranges. When combined, the Fe K-shell lines in the 6.4–7.0 keV range alone can constrain the DEM distribution in a broad range of $\gtrsim 1$ dex. In the same temperature range, H-like and He-like Si, S, Ar, and Ca K-shell lines can be easily measured and used for constraining the elemental abundance across a wide FIP range from the low (Ca) to the high (Ar) end.

3 Target and observation

3.1 Target

The observation target is an RS CVn type binary, HR 1099 (V711 Tau). It is located at a distance of ~ 29.4 pc and consists of two sub-giants: K1 IV primary and G5 IV–V secondary (Fekel 1983) with its orbital period of $P = 2.837711 \pm 0.000066$ day and an epoch of the phase origin at HJD=2457729.7084 ± 0.0017 (Strassmeier et al. 2020). The radii of the primary and secondary

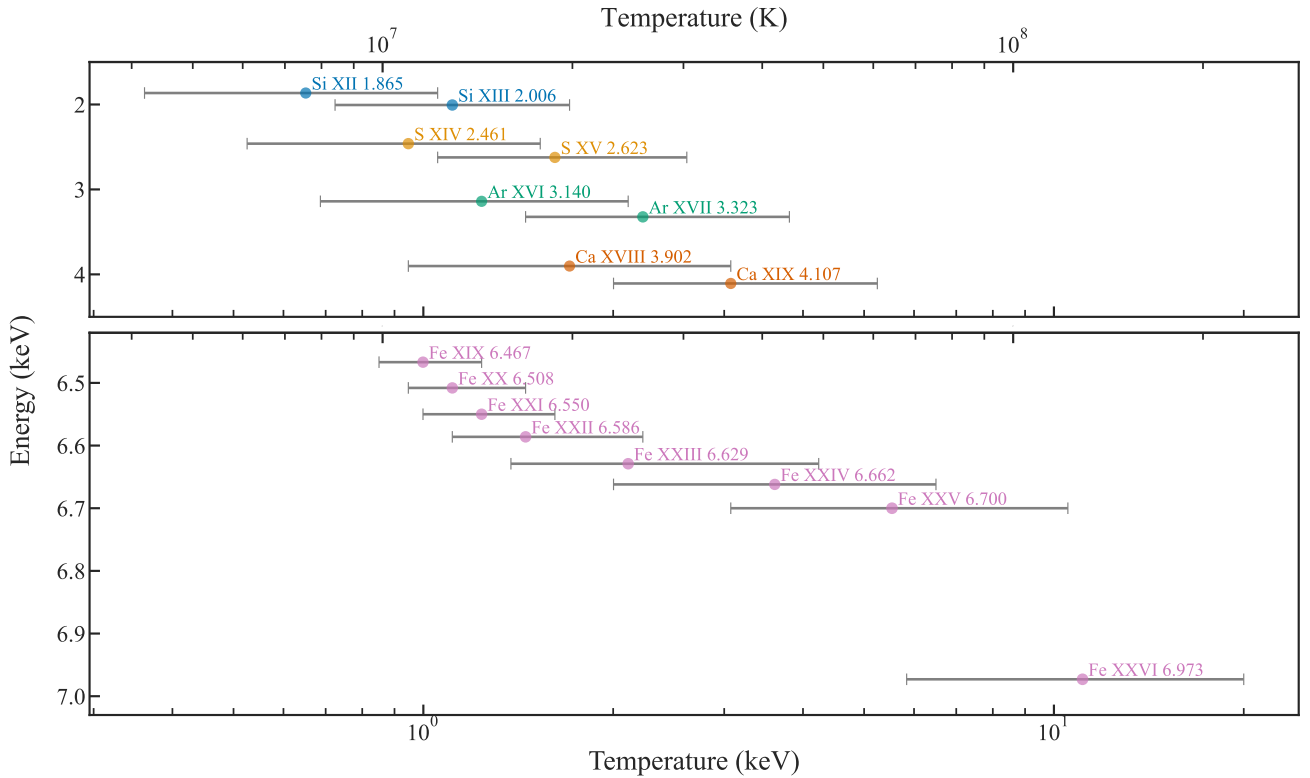


Fig. 1. Temperature range at which representative emission lines of different elements in different charge states are formed. Their ion name and the line energy in keV are given for each dot. The dots are placed at the peak of the contribution function (at the low density limit of 10^{10} cm $^{-3}$) on the horizontal axis and the line energy on the vertical axis. The horizontal bars indicate the temperature range where the contribution function exceeds half of the peak value. For Fe, selected lines of the lower charge states (Fe XIX–XXII) are predominantly formed by the dielectronic recombination process, while those of the higher charge states (Fe XXIII–XXVI) are by direct excitation. For Si, S, Ar, and Ca, the w line of the He-like and the Ly α_1 line of the H-like ions are selected. Chianti version 11 (Dere et al. 1997; Dufresne et al. 2024) is used. Alt text: A figure showing temperature ranges that Si, S, Ar, Ca, and Fe lines can cover.

stars are estimated to be $3.3 - 4.3 R_{\odot}$ and $1.1 - 1.5 R_{\odot}$, respectively, for the assumed inclination angle $30 - 40^{\circ}$ (Fekel 1983). The radial velocities with respect to the Earth have an amplitude of $K_1 = 48.47$ km s $^{-1}$ (equivalent Doppler shift of 1.4 eV at 6.7 keV) and $K_2 = 62.41$ km s $^{-1}$ (1.1 eV) with a systemic velocity of -14.76 km s $^{-1}$ (-0.33 eV).

Leveraging its proximity and brightness, extensive multi-wavelength observations have been conducted for HR 1099. The primary star is the more active, exhibiting strong chromospheric and coronal activities (Golay et al. 2024). The existence of star spots is also indicated based on Zeeman Doppler imaging (e.g., Petit et al. 2004) and photometric observations (e.g., Berdyugina & Henry 2007).

The star is also active in the X-rays (Perdelwitz et al. 2018), which is known to be predominantly from the K1 IV primary (Ayres et al. 2001). Many high-resolution X-ray spectroscopic observations were made using the grating spectrometers onboard XMM-Newton (Brinkman et al. 2001; Audard et al. 2001; Pandey & Singh 2012; Didel et al. 2024) and Chandra (Ayres et al. 2001; Nordon & Behar 2007, 2008; Huenemoerder et al. 2013; Bozzo et al. 2024), including the first-light observation of the former. Bozzo et al. (2024) revealed that the line shift follows the radial velocity change expected for the primary. From the observations during 1978–2024, the flare frequency is estimated as 57 flares

over 142-day total observing time (Didel et al. 2024). In the largest flares, the flux reached $> 5 \times 10^{-11}$ erg s $^{-1}$ cm $^{-2}$ in the 0.1–12 keV energy band and the temperature is ~ 3 keV (Audard et al. 2001; Perdelwitz et al. 2018).

3.2 Observation

For the results presented here, we used Resolve (Kelley et al. submitted; Ishisaki et al. 2025), one of the two scientific instruments onboard XRISM. Resolve is a cryogenic non-dispersive X-ray spectrometer (McCammon et al. 1984) with excellent spectroscopic performance along with a wide energy coverage of 0.3–12 keV. The energy resolution and gain accuracy are $\Delta E \sim 4.5$ eV (full width at half maximum, FWHM) and 0.3 eV, respectively in the Fe K band (Porter et al. 2024; Eckart et al. 2024). However, the energy band pass is restricted to above 1.7 keV due to the transmission of the Be window in the instrument gate valve (Midooka et al. 2021), which remains closed on orbit as of today.

The observation (sequence numbers 100011010–100011012) was conducted from 2024 March 06 1:15 to March 10 22:40. The observation was performed both for science and instrument calibration. As such, there were several additional features of this observation that enhanced the data for calibration, but had only some minor impacts on the science observation.

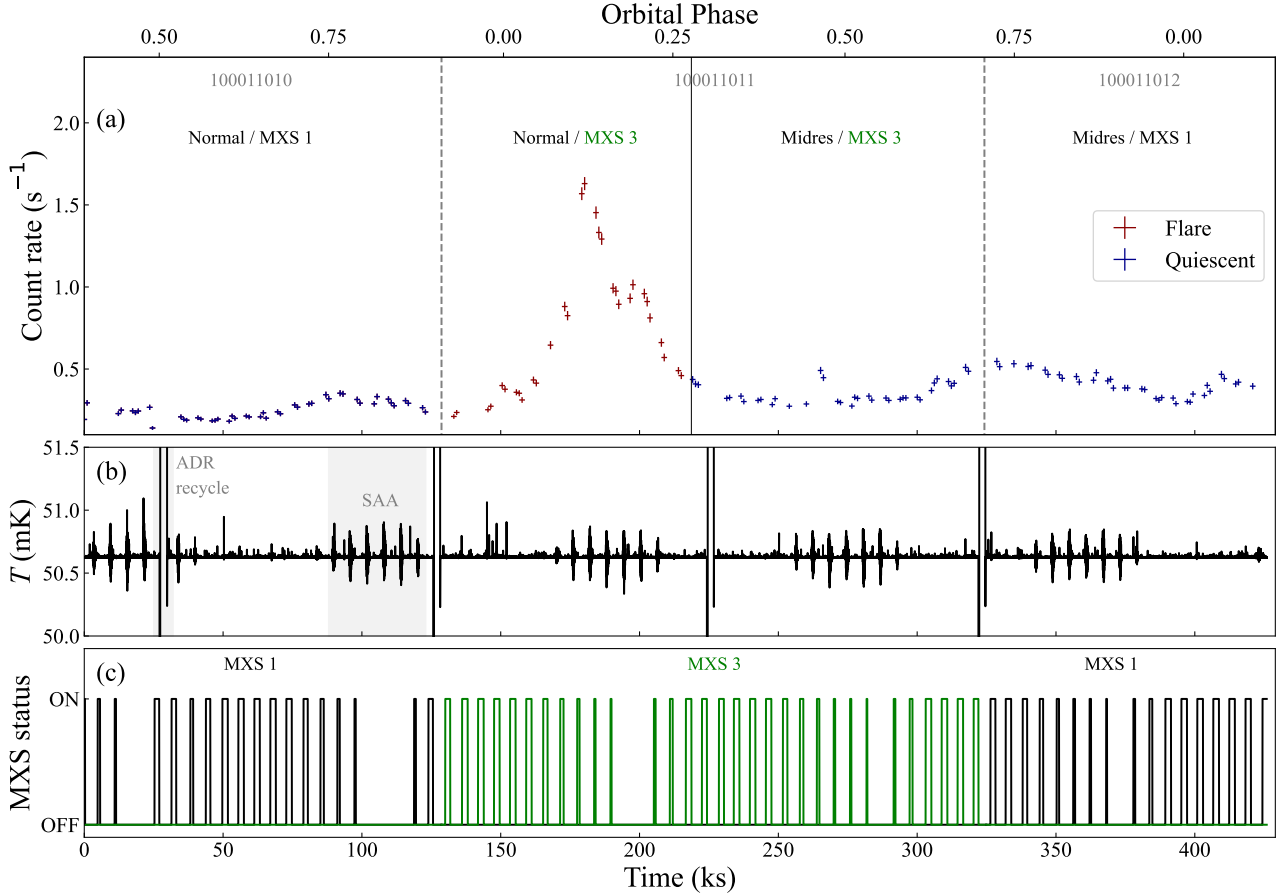


Fig. 2. (a) Resolve light curve of HR 1099 in the 1.7–10.0 keV with a 1024 s binning after good-time-interval screening. The reference time is 2024-03-06T01:15:32. The binary phase (i.e., the orbital phase of the binary, with the primary star being in front at phase zero) is shown on the top axis. The modes of the observation are shown for the four parts. The flare phase was chosen to be the same with the second part, as it encompasses most of the flare. (b) Temperature of the 50 mK stage of the detector cooling system. The four large deviations at around 25, 125, 225, and 325 ks are due to ADR recycles. Other repeated deviations are mostly due to spacecraft passages of the South Atlantic Anomaly (SAA) region. (c) Status of the MXS on or off. MXS1 is in black, while MXS3 is in green. They were turned on when the source was eclipsed by the Earth. The ^{55}Fe sources on the filter wheel were also rotated into the aperture during the same intervals. Alt text: A three-panel figure showing (a) X-ray light curve in the 1.7–10.0 keV energy range, (b) 50 mK stage temperature, and (c) MXS status during the observation.

For calibration purposes, the observation was divided into four parts. Each part was a combination of using one of the two onboard modulated X-ray calibration sources (MXS1 and MXS3) and one of two on-board processing modes (normal and “forced midres”). Briefly, the two MXS sources (de Vries et al. 2018; Shipman et al. 2024; Sawada et al. 2024) each can only illuminate about half of the focal plane array with the instrument gate valve closed, thus each one was used for half of the two processing modes. The calibration sources (MXS along with the ^{55}Fe sources on the filter wheel) were used only during Earth occultation to check the energy scale, and thus do not affect the observation of HR 1099 directly. The normal mode is for the standard processing, in which high resolution (HR) graded events are processed with HR templates onboard (Ishisaki et al. 2018). The forced midres mode is for calibration, in which HR events are processed instead with mid resolution (MR) templates, which only have a quarter of the length of HR templates. A low count rate source such as HR 1099 yields predominantly HR events. However, with the forced midres mode, we can check the energy scale for MR events indepen-

dent of count rate. The first half of this observation was performed in normal mode, and the second half in forced midres mode.

The only impacts of this calibration configuration on the science observation were: (1) half of the observation was in the forced midres mode with an average energy resolution of 4.8 eV at 6 keV, while the other half was in normal mode with an average energy resolution of 4.5 eV at 6 keV, for high-resolution graded events (Porter et al. 2024) and (2) there were much more frequent time-dependent energy scale fiducial measurements than a standard Resolve observation of typically 2–3 measurements per day with \sim 30 minutes each. This was done to build up enough statistics from the onboard calibration sources in both normal and forced midres modes to verify the time-dependent energy scale correction. However, the additional calibration periods have little effects on the science observation of HR1099 except to contribute to the verification that the Resolve in-flight calibration process is effective (Porter et al. 2024; Eckart et al. 2024).

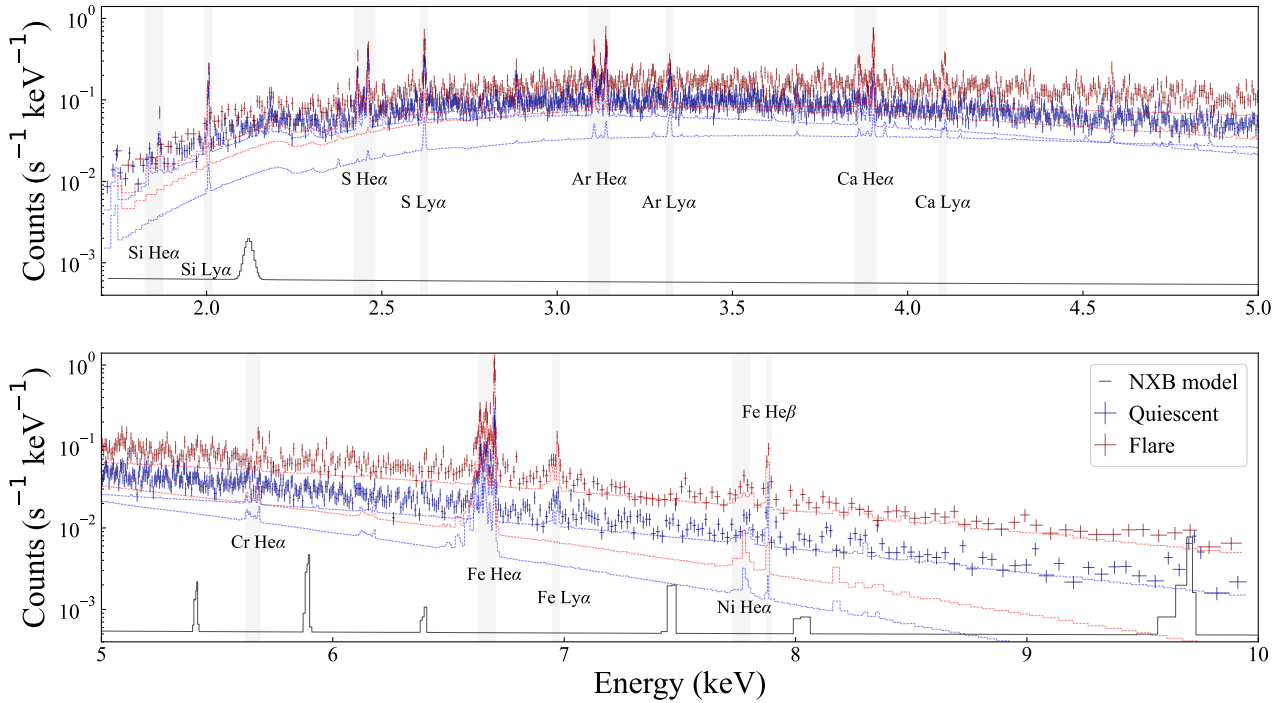


Fig. 3. Resolve spectrum in the 1.7–10.0 keV for the flaring (red) and quiescent data (blue) phase as well as the background model spectrum (black). The best-fit model of the fiducial $2kT$ fit components is also shown. The gray stripes indicate the energy range of the conspicuous He α and Ly α lines. The data were binned to have a minimum of 30 events per bin for this figure. Alt text: Resolve X-ray spectrum in the 1.7–10.0 keV range.

3.3 Data reduction

The archived data was originally processed using pipeline processing version 03.00.013.009 (Doyle et al. 2022). The data was then reprocessed using the `xipeline` ftool included in HEASoft 6.35.1 and HEASoft `XRISM_CalDB11` in the following manner to account for the non-standard instrument configuration during this observation. Separate gain history files for the normal and forced-midres parts of the observations were constructed using the gain fiducial measurements (using on-board ^{55}Fe sources in the standard method; Porter et al. 2024) independently, but in a similar manner, to that implemented in standard processing. The data in these files allow a per-pixel, time-dependent, energy-scale calibration to be applied in reprocessing using the `userghf` parameter in the `xipeline` task.

In addition, the gain curves stored in the calibration database (`XRISM_CalDB11`) were applied such that the MR gain was applied to HR events for the data acquired in forced midres mode as described above. After screening, the total on-source time was ~ 231 ks. Spectra used for analysis were extracted from cleaned event files with the following standard additional post-processing screening applied: (1) cuts based on pulse rise time and pixel-to-pixel coincidence (Mochizuki et al. 2025a) and (2) removal of all events in pixel 27, which is known to experience sudden, unpredictable gain variations. We analyze only HR grade events regardless of whether on-board processing was conducted using the HR or MR template, using the appropriate energy scale conversion and response matrices.

The `xaarfgen` and `rslmkrmf` tasks in the HEASoft version 6.35.1 were used to generate the telescope effective area function (ARF) and detector redistribution matrix file (RMF), respectively.

When some event grades are excluded from analysis, the RMF ordinarily should be scaled by the fraction of event grades kept. Resolve data, however, contain many low resolution primary (L_p) events that are induced by cosmic rays, which are followed by multiple false low resolution secondary (L_s) events by the secondary-pulse detection algorithm in the clipped L_p event. Since the rate of real L_s events from HR 1099 is negligible, we removed all L_s events prior to generating the RMF. As with the gain, HR grade events during the forced midres mode part of the observation were treated as if they were MR grade events in generating the RMF since the line spread function reflects the shorter MR grade template applied to them. The resulting ARF is consistent with that for an on-axis point source.

The non-X-ray background level was checked using the model available online¹, with its normalization determined from the observed spectrum in the 14–17 keV range. For energy binning of the observed spectra, the optimal binning method (Kaastra & Bleeker 2016) was applied, imposing a condition of a minimum of 10 counts per bin. The spectral fitting was performed to minimize the χ^2 statistics using the `xspec` software (Arnaud 1996). The uncertainties quoted here are for 90% statistical error.

4 Analysis

4.1 Light curve and spectra

The X-ray light curve for the entire observation is shown in figure 2 (a). On top of the baseline count rate ($0.25 \pm 0.07 \text{ s}^{-1}$)

¹ https://heasarc.gsfc.nasa.gov/docs/xrism/analysis/nxb/nxb_spectral_models.html

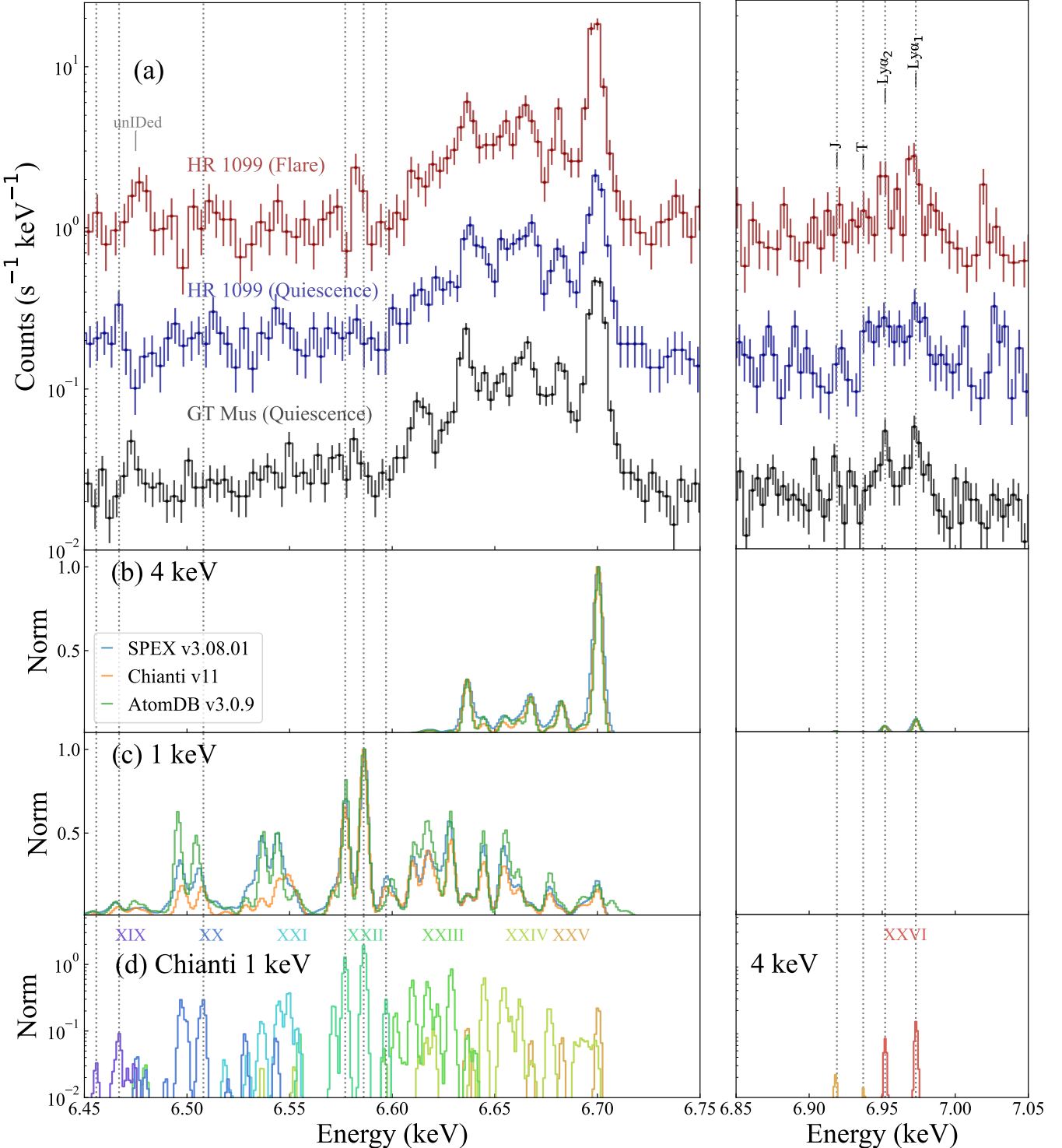


Fig. 4. (a) Close-up view of the Resolve spectra in the Fe XIX–XXVI (left) and Fe XXVI (right) K-shell complexes of HR 1099 in flare (red) and quiescence (blue) compared to that of GT Mus in quiescence (black; Kurihara et al. 2025). The intensity is scaled by $\times 20$ for the red, $\times 10$ for the blue, and $\times 1$ for the black spectra to facilitate comparison. The centroid energy of the lines used for the DEM construction is indicated by vertical dashed lines. (b, c) Synthesized spectra with three different plasma codes: SPEX version 3.08.01 (blue), Chianti version 11 (orange), and AtomDB version 3.0.9 (green) for a thermal plasma of (b) 4 keV or (c) 1 keV. The spectra are smoothed with a Gaussian of an FWHM = 4 eV, normalized at the strongest line of Fe XXVI Ly α_1 for $kT = 4$ keV and Fe XXII line 6.586 keV for $kT = 1$ keV. (d) Synthesized spectra (1 eV binning) with Chianti version 11 decomposed for each ion. Alt text: A four-panel figure of the Fe K complex of the (a) Resolve spectra, (b,c) model spectra from SPEX version 3.08.01, Chianti version 11, and AtomDB version 3.0.9, and (d) model spectra for individual ions.

Table 1. Best-fit parameters in the thermal plasma model (§ 4.2) and DEM analysis (§ 5.1.1).

Parameters	Quiescent			Flare		
	fiducial $2kT$		DEM	fiducial $2kT$		DEM
	low- kT	high- kT		low- kT	high- kT	
kT (keV)	$1.36^{+0.04}_{-0.05}$	$3.76^{+0.27}_{-0.33}$		$1.59^{+0.1}_{-0.1}$	$4.76^{+0.37}_{-0.37}$	
EM (10^{54} cm $^{-3}$)	$2.8^{+0.12}_{-0.14}$	$0.51^{+0.13}_{-0.07}$	(figure 6)	$2.8^{+0.20}_{-0.22}$	$1.0^{+0.16}_{-0.14}$	(figure 6)
Z_{Si}^*	$0.39^{+0.05}_{-0.05}$		$0.39^{+0.05}_{-0.05}$		$0.51^{+0.13}_{-0.12}$	$0.35^{+0.08}_{-0.08}$
Z_{S}^*	$0.32^{+0.03}_{-0.03}$		$0.32^{+0.02}_{-0.02}$		$0.41^{+0.06}_{-0.06}$	$0.32^{+0.04}_{-0.04}$
Z_{Ar}^*	$0.70^{+0.07}_{-0.07}$		$0.64^{+0.06}_{-0.06}$		$0.74^{+0.12}_{-0.12}$	$0.63^{+0.10}_{-0.10}$
Z_{Ca}^*	$0.55^{+0.08}_{-0.08}$		$0.49^{+0.07}_{-0.07}$		$1.13^{+0.17}_{-0.16}$	$1.00^{+0.14}_{-0.14}$
Z_{Fe}^*	$0.28^{+0.02}_{-0.02}$		$0.28^{+0.02}_{-0.02}$		$0.44^{+0.03}_{-0.03}$	$0.43^{+0.03}_{-0.03}$
Z_{Ni}^*	$0.45^{+0.33}_{-0.32}$		$0.56^{+0.36}_{-0.35}$		$0.59^{+0.38}_{-0.38}$	$0.64^{+0.38}_{-0.38}$
Reduced χ^2 (dof)	1.04 (1937)		1.05 (1941)		0.98 (1694)	1.06 (1698)

* The elemental abundances are relative to those of Wilms et al. (2000).

that varies slowly with a small amplitude, several sudden increases were found. The largest increase peaked at approximately 180 ks from the start of the observation, reaching 1.6 s^{-1} , and lasted until about 220 ks. There are several smaller events at ~ 150 , ~ 200 , and ~ 260 ks. It happened to be that the second of the four parts of the observation contained most of the largest event and two smaller events. We thus use this duration to extract the flare spectrum and all the others for the quiescent spectrum. The total radiation energy of the flare is estimated to be $\approx 10^{34}$ erg in the 1.7–10 keV range.

The Resolve spectra for the quiescent and flare phases are presented in figure 3. Both spectra exhibit a rich set of emission lines superimposed on the continuum emission, including He-like and H-like transitions from elements such as Si, S, Ar, Ca, Cr, Fe, and Ni. The flare spectrum shows a substantial increase in both continuum and line fluxes, reflecting enhanced high-temperature plasma emission during the flare. It is confirmed that the background spectrum is almost negligible, except for the Au L line at ~ 9.7 keV, thus the background spectrum was not subtracted in the spectrum fitting shown below.

4.2 Broadband spectral modeling

We first describe the entire spectrum using an emission model from the collisionally ionized plasma at a thermal equilibrium and at the optically thin and low-density limits (APEC model; Smith et al. 2001). The model parameters are the plasma temperature (kT), emission measure (EM), and elemental abundance relative to solar (Z). The abundance table in Wilms et al. (2000) was used. The model was attenuated by the photo-electric absorption model (Wilms et al. 2000) for the interstellar extinction with the H-equivalent column density (N_{H}), which is set to be 10^{18} cm $^{-2}$ by following previous studies on this target (Huenemoerder et al. 2013; Didel et al. 2024).

For both the quiescent and flare spectra, we first fitted with a single-temperature model with $kT \sim 2$ keV, which left significant residuals at both low- and high-energy ends. We then fitted with a two-temperature model with $kT < 2$ keV and $kT > 2$ keV with a common Z but with a different EM . This yielded a reasonable result (table 1). This is a traditional approach to be compared to the DEM analysis presented later, and we call this fiducial $2kT$ model hereafter.

4.3 Fe K-shell line complex modeling

4.3.1 Inspection

We start by inspecting the spectrum (figure 4a) for the Fe XIX–XXV K-shell complex (left) and Fe XXVI K-shell complexes (right). The HR 1099 spectra in the flare and the quiescence as well as the GT Mus spectrum in the quiescence are compared. GT Mus is an RS CVn type binary and is the only other stellar source observed so far with Resolve (Kurihara et al. 2025). We divide the two complexes into three bands: (1) Fe XIX–XXII K-shell band (6.450–6.603 keV), (2) Fe XXIII–XXV K-shell band (6.603–6.750 keV), and (3) Fe XXVI K-shell band (6.850–7.050 keV). A list of lines in each band is provided in table 2 with their conventional labels, if any, ion, lower and upper levels, and line center energy. These lines carry rich information for the DEM construction.

In the Fe XXVI K-shell band, the main lines of Fe XXVI as well as the dielectronic recombination (DR) satellite lines of Fe XXV are included. The Fe XXVI Ly α_1 and Ly α_2 (6.973 and 6.952 keV) lines probe the electron distribution around ~ 5 keV. They can be seen in both phases and appears enhanced during the flaring phase (figure 4). The clear separation of Ly α_1 and Ly α_2 and the major DR lines J and T requires the spectral resolution $R \gtrsim 500$ in this band, which is unique to Resolve among X-ray spectrometers for stellar sources.

In the Fe XXIII–XXV K-shell band, the main lines of Fe XXV (w : 6.700, x : 6.683, y : 6.668, and z : 6.637 keV) as well as the satellite lines of Fe XXIII–XXIV (q : 6.662, j : 6.645 keV, etc) are included. The satellite to main line ratio is a robust estimator of the electron temperature due to their different line formation processes as was demonstrated for GT Mus with Resolve (Kurihara et al. 2025). For example, the upper level of the w line is predominantly populated via the electron collision excitation of He-like Fe, that of the q line is via the electron collision excitation of Li-like Fe, and that of the j line is via the DR of He-like Fe (Mochizuki et al. 2025b). A quick comparison of the nearby q and y lines indicates the change of the Fe charge state distribution, hence the DEM distribution.

In the Fe XIX–XXII K-shell band, the Fe K-shell lines of lower ionization stages are included. The access to these lines is also unique to Resolve for stellar sources. The lines below Fe XXI have been rarely investigated even in the Sun (Doschek et al. 1981). Since some lines are clearly detected and identified in Resolve spectra, we try to use them to constrain the temperature around ~ 1 keV (figure 1).

Table 2. Line list for the phenomenological model (§ 4.3) and the results of DEM analysis (§ 5.1.1).

Label*	Ion	Lower	Upper	E^{\dagger} (keV)	Quiescent			Flare		
					Det. [‡]	Norm (10^{-6}) [§]	Ratio	Det. [‡]	Norm (10^{-6}) [§]	Ratio
(Fe XIX–XXII K-shell band)										
Fe XIX	$1s^2.2s^2.2p^4\ 3P_1$	$1s.2s^2.2p^5\ 3P_2$	6.4558	U	< 0.90	—	—	U	< 1.2	—
Fe XIX	$1s^2.2s^2.2p^4\ 3P_2$	$1s.2s^2.2p^5\ 3P_2$	6.4669	Y	$0.12^{+0.3}_{-0.1}$	$0.9^{+0.7}_{-0.7}$	—	U	< 2.0	—
Fe XX	$2s^2.2p^3\ 4S_{3/2}$	$1s.2s^2.2p^4\ 4P_{5/2}$	6.4971	U	< 0.56	—	—	N	—	—
Fe XX	$2s^2.2p^3\ 4S_{3/2}$	$1s.2s^2.2p^4\ 4P_{1/2}$	6.5080	Y	$0.41^{+0.4}_{-0.4}$	$1.3^{+1.0}_{-1.0}$	—	U	< 1.9	—
Fe XXII	$1s^2.2s^2.2p^2\ 2P_{3/2}$	$1s.2s^2.2p^2\ 2D_{5/2}$	6.5771	Y	$0.49^{+0.4}_{-0.4}$	$0.84^{+0.6}_{-0.6}$	—	U	< 0.97	—
Fe XXII	$1s^2.2s^2.2p\ 2P_{1/2}$	$1s.2s^2.2p^2\ 2D_{3/2}$	6.5861	U	< 0.55	—	—	Y	$2.2^{+1.3}_{-1.3}$	$0.90^{+0.6}_{-0.6}$
Fe XXII	$1s^2.2s^2.2p\ 2P_{3/2}$	$1s.2s^2.2p^2\ 2S_{1/2}$	6.5970	Y	$0.46^{+0.4}_{-0.4}$	$3.0^{+2.5}_{-2.5}$	—	U	< 1.5	—
(Fe XXIII–XXV K-shell band)										
E12	Fe XXIII	$1s^2.2s.2p\ 3P_2$	$1s.2s.2p^2\ 3D_3$	6.6097	Y	$0.90^{+0.5}_{-0.5}$	$12^{+6.4}_{-6.9}$	Y	$2.1^{+1.4}_{-1.5}$	$1.6^{+1.1}_{-1.1}$
<i>u</i> [#]	Fe XXIV	$1s^2.2s^2\ 2S_{1/2}$	$1s.2s(3S).2p\ 4P_{3/2}$	6.6167	N	—	—	U	< 2.7	—
<i>e</i> [#]	Fe XXIV	$1s^2.2p\ 2P_{3/2}$	$1s.2p^2(3P)\ 4P_{5/2}$	6.6203	Y	$1.4^{+0.5}_{-1.0}$	$2.9^{+1.1}_{-2.0}$	Y	$3.0^{+1.6}_{-2.6}$	$2.6^{+1.4}_{-2.3}$
<i>E3</i> (β)	Fe XXIII	$1s^2.2s^2\ 1S_0$	$1s.2s^2.2p\ 1P_1$	6.6288	Y	$0.95^{+0.6}_{-0.6}$	$0.90^{+0.5}_{-0.6}$	Y	$3.9^{+1.8}_{-1.8}$	$1.8^{+0.8}_{-0.8}$
<i>z</i>	Fe XXV	$1s^2\ 1S_0$	$1s.2s\ 3S_1$	6.6366	Y	$3.7^{+0.8}_{-0.8}$	$1.1^{+0.2}_{-0.2}$	Y	$10.5^{+2.4}_{-2.3}$	$0.85^{+0.2}_{-0.2}$
<i>j</i>	Fe XXIV	$1s^2.2p\ 2P_{3/2}$	$1s.2p^2(1D)\ 2D_{5/2}$	6.6447	Y	$2.4^{+0.7}_{-0.8}$	$0.83^{+0.2}_{-0.3}$	Y	$5.1^{+1.9}_{-2.0}$	$0.76^{+0.3}_{-0.3}$
<i>r</i>	Fe XXIV	$1s^2.2s\ 2S_{1/2}$	$1s.2s(1S).2p\ 2P_{1/2}$	6.6529	U	< 2.4	—	U	< 7.8	—
<i>k</i>	Fe XXIV	$1s^2.2p\ 2P_{1/2}$	$1s.2p^2(1D)\ 2D_{3/2}$	6.6547	U	< 3.6	—	U	< 9.0	—
<i>a</i>	Fe XXIV	$1s^2.2p\ 2P_{3/2}$	$1s.2p^2(3P)\ 2P_{3/2}$	6.6579	N	—	—	N	—	—
<i>q</i>	Fe XXIV	$1s^2.2s\ 2S_{1/2}$	$1s.2s(3S).2p\ 2P_{3/2}$	6.6622	Y	$2.2^{+0.9}_{-2.0}$	$1.2^{+0.5}_{-1.1}$	Y	$5.6^{+2.5}_{-2.6}$	$1.2^{+0.5}_{-0.6}$
<i>y</i>	Fe XXV	$1s^2\ 1S_0$	$1s.2p\ 3P_1$	6.6676	Y	$3.7^{+1.3}_{-0.9}$	$1.6^{+0.6}_{-0.4}$	Y	$9.3^{+2.6}_{-2.4}$	$1.1^{+0.3}_{-0.3}$
<i>t</i> [#]	Fe XXIV	$1s^2.2s\ 2S_{1/2}$	$1s.2s(3S).2p\ 2P_{1/2}$	6.6762	Y	$0.90^{+0.6}_{-0.4}$	$0.98^{+0.7}_{-0.5}$	Y	$1.8^{+1.6}_{-1.7}$	$0.79^{+0.7}_{-0.78}$
<i>x</i>	Fe XXV	$1s^2\ 1S_0$	$1s.2p\ 3P_2$	6.6827	Y	$2.5^{+0.9}_{-0.7}$	$1.1^{+0.4}_{-0.3}$	Y	$7.6^{+2.2}_{-2.4}$	$0.97^{+0.3}_{-0.3}$
<i>d13</i>	Fe XXIV	$1s^2.3p\ 2P_{3/2}$	$1s.2p(1P).3p\ 2D_{5/2}$	6.6892	N	—	—	Y	$0.32^{+3.1}_{-0.3}$	—
<i>d15</i>	Fe XXIV	$1s^2.3p\ 2P_{1/2}$	$1s.2p(1P).3p\ 2D_{3/2}$	6.6917	U	< 1.9	—	Y	$2.1^{+2.1}_{-2.0}$	—
<i>w</i>	Fe XXV	$1s^2\ 1S_0$	$1s.2p\ 1P_1$	6.7004	Y	$9.6^{+1.3}_{-1.2}$	$0.94^{+0.1}_{-0.1}$	Y	$41.1^{+4.1}_{-4.1}$	$1.1^{+0.1}_{-0.1}$
(Fe XXVI K-shell band)										
<i>J</i>	Fe XXV	$1s.2p\ 1P_1$	$2p^2\ 1D_2$	6.9188	N	—	—	U	< 1.8	—
<i>T</i>	Fe XXV	$1s.2s\ 1S_0$	$2s.2p\ 1P_1$	6.9373	U	< 0.45	—	U	< 2.3	—
<i>Lya</i> ₂	Fe XXVI	$1s^2\ 2S_{1/2}$	$2p\ 2P_{1/2}$	6.9521	Y	$1.3^{+0.6}_{-0.6}$	$1.3^{+0.6}_{-0.6}$	Y	$3.3^{+1.5}_{-1.5}$	$0.99^{+0.5}_{-0.4}$
<i>Lya</i> ₁	Fe XXVI	$1s^2\ 2S_{1/2}$	$2p\ 2P_{3/2}$	6.9732	Y	$1.4^{+0.6}_{-0.6}$	$0.89^{+0.4}_{-0.4}$	Y	$5.4^{+1.8}_{-1.7}$	$0.96^{+0.3}_{-0.3}$

* Notations are from Beiersdorfer et al. (1993) for Fe XXIII lines, Gabriel (1972) for Fe XXIV $n = 2 \rightarrow 1$ lines, and Safronova's (Bitter et al. 1984) for Fe XXV satellite lines.

[†] Line energy from Chianti version 11 (Dere et al. 1997; Dufresne et al. 2024).

[‡] Whether the line is detected with a 90% significance: "Y" (detected), "U" (not detected, but an upper limit is estimated to be above the NXB level), "N" (not detected, and an upper limit is lower than the NXB level).

[§] The best-fit Gaussian norm values of the phenomenological fit.

^{||} The ratio of the input from best-fit phenomenological modeling (§ 4.3) over the DEM analysis output (§ 5.1.1). Those from lines not used in the DEM analysis are indicated with "—".

Lines with possible blending with others commented in Beiersdorfer et al. (1993): *u* with (Fe XXIV *v*, Fe XXIII *E8*, and Fe XXIII *E9*), *e* with (Fe XXIII *E6* and Fe XXIII *E7*), and *t* with Fe XXIV *m*.

Table 3. Best-fit parameters in the phenomenological model (§ 4.3).

Parameter	Quiescent			Flare		
	Fe XIX–XXII K-shell	Fe XXIII–XXV K-shell	Fe XXVI K-shell	Fe XIX–XXII K-shell	Fe XXIII–XXV K-shell	Fe XXVI K-shell
Redshift (eV)	Fixed*	$0.0^{+0.5}_{-0.5}$	Fixed*	Fixed*	$1.0^{+0.3}_{-0.3}$	$1.6^{+1.0}_{-1.0}$
Broadening (eV)	Fixed*	$2.5^{+0.7}_{-0.6}$	$6.2^{+3.8}_{-2.4}$	Fixed*	$2.1^{+0.4}_{-0.4}$	$2.4^{+1.4}_{-1.3}$
Reduced χ^2 (dof)	1.41 (35)	0.67 (26)	1.18 (40)	1.24 (30)	0.90 (24)	0.82 (36)

* The value is fixed to the best-fit value in the high He α band in the same phase.

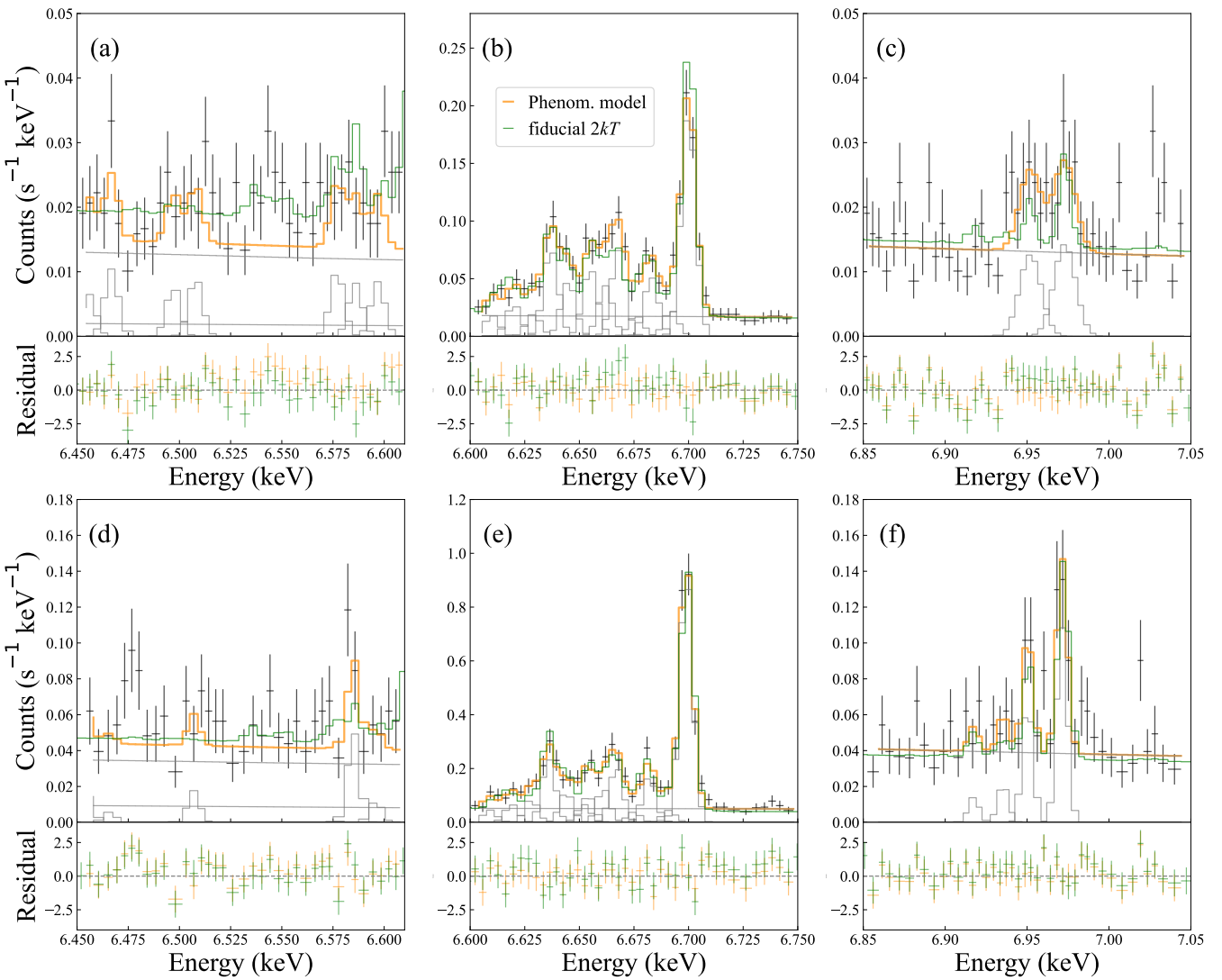


Fig. 5. Close-up views of the Resolve spectrum (black) of the Fe K-shell line complexes, the best-fit model with the fiducial $2kT$ model (green) and phenomenological model (orange), and their residuals. The upper panels (a)–(c) are for the quiescent spectrum, while the lower panels (d)–(f) are for the flare spectrum. Alt text: A pair of three-panel figures showing close-up views of the Resolve spectra in the Fe K-shell line complexes and the best-fit spectral models for the quiescent and flaring phases, respectively.

4.3.2 Fitting

We fitted the spectrum in each band using a phenomenological model, which consists of lines listed in table 2 upon the continuum emission. The individual lines are represented with a Gaussian model with a fixed energy based on Chianti version 11 (Dere et al. 1997; Dufresne et al. 2024) and a normalization as a free parameter. All lines are collectively fitted for the parameters of the energy shift and the broadening. The continuum emission is represented by the NLAPC model (Smith et al. 2001), which is equivalent to the APEC model for thermal plasma emission but without emission lines having emissivities larger than $10^{-20} \text{ cm}^3 \text{ s}^{-1}$. The best-fit model is illustrated in figure 5, while the best-fit parameters are tabulated in tables 2 and 3. We also checked the possibility of the plasma deviating from a collisionally ionized equilibrium using the ratios of the Fe XXVI Ly α_1 , Fe XXV w and J , Fe XXIV j and q (Kurihara et al. 2025), which yielded no conclusive evidence for any deviations.

A redshift of $50 \pm 15 \text{ km s}^{-1}$ was observed during the flare (ta-

ble 3). The sign of the observed radial velocity is consistent with that expected from the orbital motion of the primary star (Bozzo et al. 2024) at around phase = 0.1, when the flare reached its peak, although the measured velocity shift is somewhat larger. The difference may be attributable to additional kinematic effects associated with the flare, such as chromospheric evaporation and/or coronal mass ejection (Inoue et al. 2024), as well as to the relative motion of the satellite with respect to the system. The limited statistics do not allow us to investigate this further, and will be left out of the scope of this study.

5 Discussion

5.1 DEM distribution

5.1.1 Choice of lines

We first consider which lines to use for the DEM construction. Those in the Fe XXIII–XXV K-shell and Fe XXVI K-shell bands are relatively straight-forward and well established in ground experi-

ments (Beiersdorfer et al. 1993; Decaux et al. 1997; Rudolph et al. 2013) and solar observations (e.g., Phillips et al. 2004; Watanabe 2024) and are used with Resolve (Kurihara et al. 2025). In contrast, those in Fe XIX–XXII K-shell band are less established even in ground experiments and solar observations and are new with Resolve.

We compared three different plasma codes —Chianti version 11 (Dere et al. 1997; Dufresne et al. 2024), AtomDB version 3.0.9 (Smith et al. 2001; Foster et al. 2012) and SPEX version 3.08.01 (Kaastra et al. 1996, 2024)— in figure 4 (b). Their synthesized spectra exhibit larger discrepancies in the Fe XIX–XXII K-shell band than the other two bands, suggesting the level of systematics. All three codes were compared to the Hitomi observation of the Perseus cluster using the X-ray microcalorimeter (Hitomi Collaboration et al. 2018). Among the three codes, Chianti is the most well-verified with solar observations, but still has significant limitations, especially for the lower charge states. The model of Fe XVIII–XXIII was updated in version 9, although comparisons with solar observations were made only for Fe XXII and the higher charge states (Dere et al. 2019). Two results illustrate the limitation. One is that some strong lines of the lower charge states (Fe XIX and XX) were observed during solar flares (Phillips 2004; Feldman et al. 2006), but they do not match with Chianti in line center or strength. The other is that a clear but unidentified line feature at \sim 6.475 keV was observed in the Resolve data of HR 1099 during the flare, which might also be present in the GT Mus data (figure 4a). The line is too strong to be a Fe XIX–XXI line, or an Fe XXIII line that exists around 6.479 keV (figure 4c). We also confirmed that the line does not match with known lines of He- or H-like ions of Cr and Mn including their Rydberg series (Hell et al. 2025 and references therein).

Considering all these, we decided to use all detected lines in the Fe XXVI K-shell and Fe XXIII–XXV K-shell bands except for the Fe XXIV *d*15 in the flaring phases (as it belongs to the unresolved infinite series of DR transitions onto levels with $n \geq 3$), and some strong and relatively isolated detected lines in the Fe XIX–XXII K-shell band for the Fe XXII, XX, and XIX that have corresponding structures found by eye in Resolve spectra. The Fe XXI lines were not used, as nearby lines from other charge states, especially Fe XXIV *o* and *p* are present with possible large contributions from high-*kT* components.

5.1.2 DEM construction

There are two major approaches conventionally used to model the temperature structure of the stellar corona in X-ray spectroscopy. One is to describe the global spectra using multiple discrete temperature components, which is often used in medium-resolution CCD spectra. This method is advantageous for the use of both the line and continuum emission, which is useful in particular when the Bremsstrahlung cutoff lies within the spectrum range. The other is to account for individual line intensities with pre-calculated contribution functions, which is often used in high-resolution grating spectra both in solar and stellar studies. This allows us to constrain parametric or even non-parametric models of the DEM distribution directly from the fitting. In this paper, we adopt the latter approach, which was made possible by the increased number of resolved Fe K-shell lines with Resolve.

Several techniques have been developed for constructing DEM distributions in solar studies (Del Zanna & Mason 2018 for review). Typically, these represent a compromise between allowing significant structure in the DEM to attempt to maximize the number of line intensities that can be reproduced, and adding smooth-

ing to the DEM to try to capture a more physically realistic temperature distribution. After an initial survey of the Resolve dataset using a variety of techniques, we decided to adopt the method introduced by Warren (2005) for solar EUV spectra. In this technique, the DEM distribution is parameterized with a spline function of the temperature. The parameters are constrained through χ^2 fitting of the line intensities using the contribution functions calculated with Chianti. This approach provides improved flexibility in reproducing the steep decline in the DEM distribution at the highest temperature end, a behavior that, as we show below, is visible in the HR 1099 data, and other multi-temperature fitting approaches often struggle to capture.

We first derived the shape of the DEM distribution using only the Fe K lines selected in § 5.1.1. We then determined the scaling factor of the DEM distribution by referring back to the observed spectra in the 1.7–10.0 keV band for the purpose of decoupling the degeneracy between the normalization of the DEM distribution and the Fe abundance. The DEM model spectra were synthesized by summing APEC models with the corresponding temperatures and emission measures. After adjusting the abundances of the other elements and the overall normalization, the DEM model yielded fit statistics comparable to those of the fiducial $2kT$ models, as shown in table 1.

5.1.3 Result

Figure 6 presents the DEM distributions derived with uncertainties separately for the quiescent and flare phases. We assessed the success of our analysis by examining the reproduction rate of each line, defined as the ratio of the synthesized line intensity to the observed line intensity, for each DEM distribution (table 2). This is expected to be unity, which is satisfied for most lines within the statistical uncertainty. A few exceptions are Fe XXIII *E*12, Fe XXV *y*, and *w* during the quiescent phase, which may be attributable to blending with neighboring lines. Nevertheless, a sufficiently large number of lines were successfully used to constrain the DEM distribution over the 1–10 keV temperature range.

The DEM exhibits a bimodal distribution both for the quiescent and flare phases peaking at \sim 1 and \sim 5 keV. The hotter component of the two increased during the flare, while the colder component remained almost unchanged. Although the temperature range is shifted higher in HR 1099, the bimodal distribution is often observed when the Sun is viewed as a star (e.g., Caspi et al. 2014 and references therein). The valley in the DEM distribution at \sim 3 keV stems from the observed weakness of the Fe XXIV line intensities compared to the other Fe lines; they would have been stronger if the DEM distribution was flat across \sim 3 keV. Such a constraint is difficult to obtain in the traditional multi-*kT* modeling, as the χ^2 local minimum can be easily obtained without accounting for weak lines.

5.1.4 Comparison

We compared the DEM distribution of HR 1099 in previous results using HETG during quiescence (Huenemoerder et al. 2013) and in a flare (Nordon & Behar 2008) and that using RGS in both flare and quiescence (Audard et al. 2001). The distributions in Huenemoerder et al. (2013) and Audard et al. (2001) are shown in figure 6. The DEM distributions are somewhat different from one another. While the distributions in the two HETG and RGS quiescent phase results are roughly single-peaked, that in the Resolve results shows a double peak. In the solar case, multiple-peaked DEM distributions have been shown to arise from a number of uncertainties (Lanzafame et al. 2002), and we list several possible

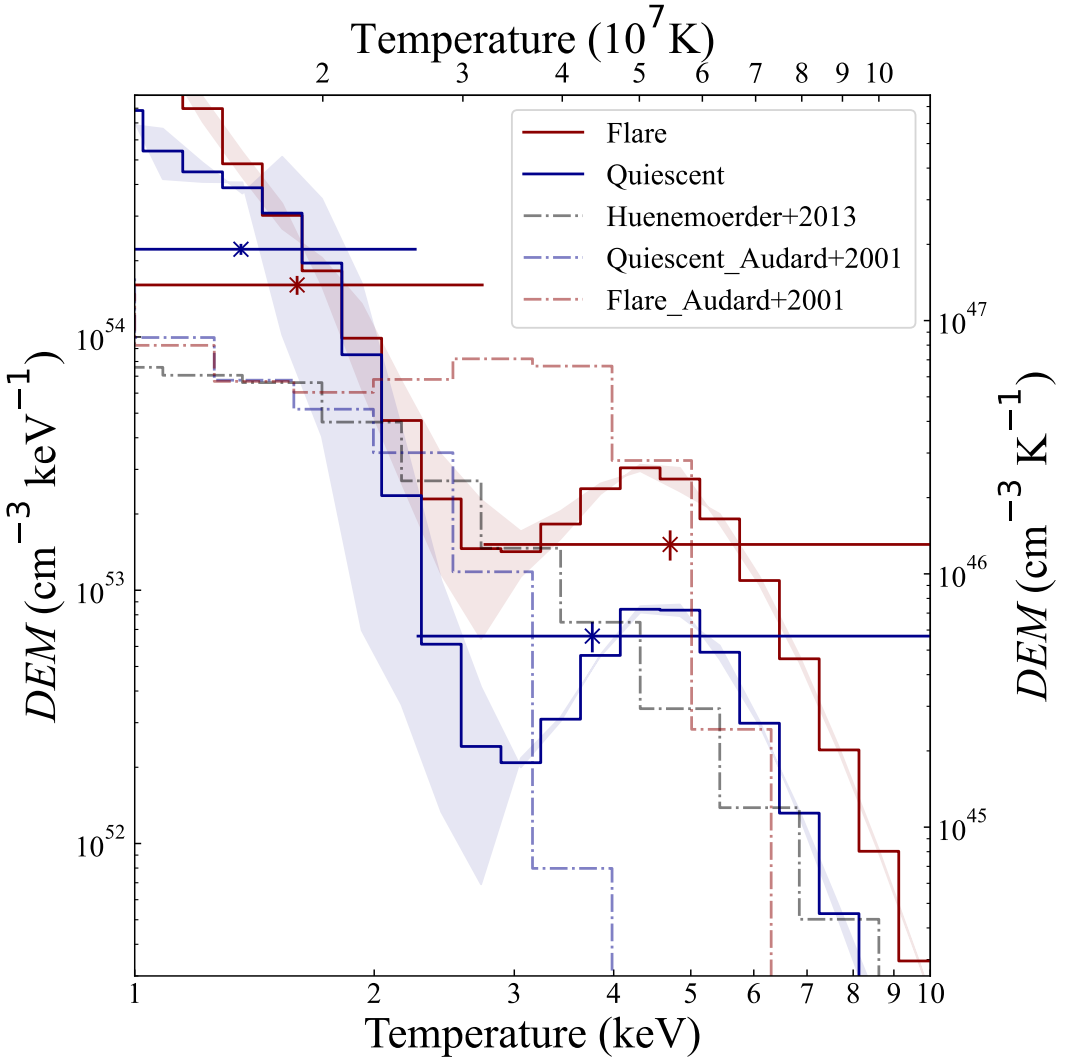


Fig. 6. DEM (histogram with errors) derived from the series of Fe K-shell lines for the quiescent (blue) and flaring (red) phases. Discrete data points indicate the DEM derived from the fiducial $2kT$ model, and their horizontal error bars are divided by the geometric means of the two best-fit temperatures at each phase. A DEM derived in the previous studies are also shown: Huenemoerder et al. (2013) using Chandra in gray, Audard et al. (2001) using XMM-Newton for quiescence in dashed blue and flare in dashed red, respectively. Alt text: A figure showing DEM for the quiescent and the flaring phases as well as one from the previous studies.

additional reasons for the difference here. The first is that the DEM depends on how it is reconstructed. For instance, the RGS result in the quiescent phase is based on the traditional multi- kT approach, while the two HETG results are derived from individual line fitting based on contribution functions. The second is that RGS and HETG lack sensitivity to the lines of Fe xxv, Fe xxvi, or both. Third, the flare in the HETG observation (Nordon & Behar 2008) is much weaker than the one detected with Resolve or RGS; the count rate increased only by 10%. In fact, a small increase at 260 ks from the start in the Resolve data (figure 2), which we recognized as a part of quiescence, is larger than the flare in Nordon & Behar (2008). The quiescent phase in Huenemoerder et al. (2013) has some variation within a factor of 2 in the light curve (Ayres et al. 2001). In large stellar flares in other stars observed with grating spectrometers, the bimodal DEM distribution and the increase only of the hotter component appears to be the norm, as was seen in σ Gem (Nordon et al. 2006; Huenemoerder et al. 2013), and AD Leo (Van den Besselaar et al. 2003).

5.2 Abundance

Based on the DEM distribution derived solely from the Fe K-shell lines, we estimated the abundances of the other elements. While the relative shape of the DEM was fixed, allowing the vertical scaling to vary, we fitted the abundances of Si, S, Ar, Ca, Fe, and Ni relative to H, together with the DEM normalization, to the 1.7–10 keV spectra. In practice, we use the continuum level, which includes free-free, free-bound, and two-photon emission (with a dominant contribution from hydrogen free-free), primarily as a proxy for the H abundance. The results are summarized in table 1, while the abundance as a function of the FIP is depicted in figure 7 (a). The reference values of FIP are retrieved from NIST Atomic Spectra Database (Kramida et al. 2024). Since we do not know the photospheric abundances of stars such as HR 1099, it is common to interpret their spectra using solar photospheric abundances. During the quiescent phase, the observed abundance pattern of Fe, Si, S, and Ar is consistent with previous results for HR 1099 (see figure 7 in Didel et al. 2024). Overall, the elemental abundances

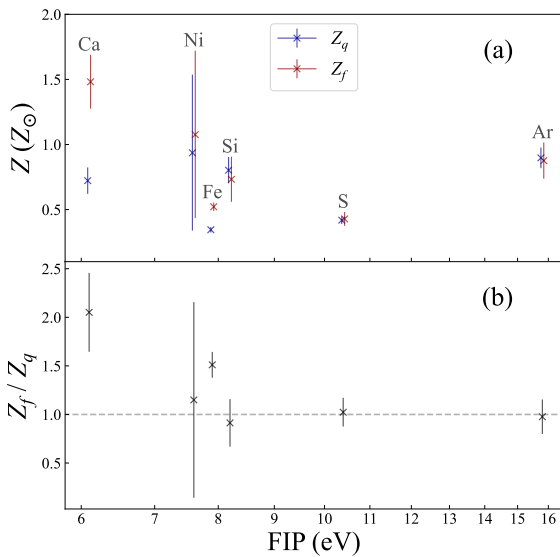


Fig. 7. (a) Derived elemental abundance of the quiescent (blue) and the flare (red) phase. The abundance values relative to those of Wilms et al. (2000) are plotted against the FIP. (b) Ratio between the quiescent and flare abundances. Alt text: A two-panel figure showing the measured abundances.

are sub-solar photospheric, though the photospheric abundances of HR 1099 may differ from the solar values.

We thus focus on the relative abundances in the flare phase compared to the quiescent phase within our dataset (figure 7b). During the flare, the abundances of Ca and Fe increased clearly by a factor of ~ 2 for Ca and $\sim 50\%$ for Fe, while those of the other elements remained unchanged. This selective enhancement can be understood as follows. As Nordon & Behar (2008) suggested in their stellar flare studies and as confirmed also in solar flares (e.g., Warren 2014), chromospheric evaporation (Neupert 1968; Güdel et al. 2002) can transport plasma with different chemical compositions than those in the coronae into the flare loop. The fact that HR 1099 nominally exhibits the i-FIP effect and only the two elements with the lowest FIP in our sample showed enhancement during the flare provides support for the evaporation scenario. In solar studies, Si is often regarded as a low-FIP element, but no significant variation was detected here. It is unclear whether this reflects the diverse nature of the FIP effect or an observational bias, given that the $\text{He}\alpha$ features of Si lie close to the lower end of the energy band, unlike those of the other elements.

One proposed explanation for the FIP fractionation is the ponderomotive force, which acts only on charged particles (Laming 2015, 2021). In this context, Ca is particularly interesting: it has a low first ionization potential (6.1 eV) and a second ionization potential (11.9 eV), making it the only abundant element whose second ionization potential lies below the first ionization potential of H (13.6 eV). Observational evidence for the relative enhancement of elements with lower FIP than Fe has so far been scarce in stellar cases (e.g., Mg in AT Mic; Raassen et al. 2003), despite many reports of abundance variations during flares in general (e.g., Favata & Schmitt 1999; Nordon & Behar 2007, 2008; Liefke et al. 2010). This first detection of Ca enhancement pre-

sented here demonstrates the complementary spectroscopic capabilities of XRISM to the grating missions, highlighting its value in probing the diverse manifestations of the FIP effect in stars.

To investigate this further, we should make assessments similar to figure 7 (b) in more elements, including larger stellar flares. When a giant solar flare is resolved temporally, or spatially, or both, or an in-situ measurement is employed, an increase of the low-FIP elements can be observed at some times, or in some locations, such as the initial phase of the flare, at the loop top, or in the slow wind (Katsuda et al. 2020; Suzuki et al. submitted; To et al. 2024; Brooks et al. 2022). With better photon statistics, time-resolved spectroscopy will enable comparisons with the Sun as well as the reduction of observational bias due to the lack of spatial resolution. Furthermore, giant flares may allow the detection of very low-FIP elements of alkali metals such as Na (5.1 eV) and K (4.3 eV) with high-resolution X-ray spectroscopy, despite their small abundances (Huenemoerder et al. 2013). As is demonstrated by previous results with grating spectrometers and the present result with the microcalorimeter spectrometer, we now have instruments and diagnostic tools to make this possible. Investments of long telescope times to capture flares are awaited in the future.

6 Summary

We presented the result of the Resolve observation of an RS CVn star HR1099. A stellar flare was observed with an X-ray microcalorimeter for the first time. In addition to the $\text{Fe He}\alpha$ and $\text{Ly}\alpha$ complexes modeled in our previous study of GT Mus with Resolve (Kurihara et al. 2025), lines from relatively lower charge states of Fe XIX-XXIII were utilized for the reconstruction of the DEM distribution, effectively extending Fe K-shell diagnostics pioneered by solar missions such as P78-1 (Doschek et al. 1979), the Solar Maximum Mission (SMM; Culhane et al. 1981), and Hinotori (Tanaka et al. 1982). The DEM was derived using a single element, Fe, for both the quiescent and flaring phases, covering a temperature range from $\sim 1-10$ keV. We found that the DEM distribution is bimodal, and only the hotter component increased during the flare. Based on the DEM distribution thus obtained, the elemental abundances of Si, S, Ar, Ca, Fe, and Ni were derived. The observed increase of abundances only at the lower end of the FIP range (Ca, Fe) constitutes a clear example of the abundance change during stellar flares as a function of the FIP. Along with previous results using grating spectrometers, we demonstrated the possibility of using X-ray high-resolution spectroscopy to investigate the chemical fractionation processes in the context of coronal heating and flare physics.

Acknowledgments

This article is published in PASJ as open access, published by OUP (<https://doi.org/10.1093/pasj/psaf124>).

We thank the anonymous reviewer for their constructive comments that helped improve the manuscript. We gratefully acknowledge insightful discussion with Tetsuya Watanabe (NAOJ) on high-resolution X-ray spectroscopy, and with Andy S. H. To (ESTEC) on solar observations of the abundance variation during flares. David P. Huenemoerder (MIT) provided the Chandra result for figure 6. This research has made use of data and/or software provided by the High Energy Astrophysics Science Archive Research Center (HEASARC), which is a service of the Astrophysics Science Division at NASA/GSFC. Chianti is

a collaborative project involving George Mason University, the University of Michigan (USA), University of Cambridge (UK) and NASA Goddard Space Flight Center (USA). This research was supported by the grant of Joint Research by the National Institutes of Natural Sciences (NINS program No OML032402). The material is based upon work supported by NASA under award number 80GSFC21M0002. M. K. was supported by JSPS Grant-in-Aid for JSPS fellows 25KJ0926 and the IGPEES, WINGS Program, the University of Tokyo, and the ACME project, which has received funding from the European Union's Horizon Europe Research and Innovation programme under Grant Agreement No 101131928. E. B. acknowledges support from NASA grants 80NSSC20K0733, 80NSSC24K1148, and 80NSSC24K1774. Part of this work was performed under the auspices of the U.S. Department of Energy by Lawrence Livermore National Laboratory under Contract DE-AC52-07NA27344. The work of D.H.B. was performed under contract to the Naval Research Laboratory and was funded by the NASA Hinode program.

References

Arnaud, K. 1996, in Astronomical Data Analysis Software and Systems V, ASP Conference Series, Vol. 101, 1996, George H. Jacoby and Jeannette Barnes, eds., p. 17., Vol. 101, 17

Audard, M., Güdel, M., & Mewe, R. 2001, *A&A*, 365, L318

Audard, M., Güdel, M., Sres, A., Raassen, A., & Mewe, R. 2003, *A&A*, 398, 1137

Ayres, T. R., Brown, A., Osten, R. A., et al. 2001, *ApJ*, 549, 554

Beiersdorfer, P., Phillips, T., Jacobs, V., et al. 1993, *ApJ*, 409, 846

Benz, A. O. & Güdel, M. 2010, *ARA&A*, 48, 241

Berdugina, S. V. & Henry, G. W. 2007, *ApJ*, 659, L157

Bitter, M., Von Goeler, S., Cohen, S., et al. 1984, *Physical Review A*, 29, 661

Bozzo, E., Huenemoerder, D., Falanga, M., et al. 2024, *MNRAS*, 528, 4591

Brinkman, A., Behar, E., Güdel, M., et al. 2001, *A&A*, 365, L324

Brooks, D. H., Baker, D., van Driel-Gesztesy, L., Warren, H. P., & Yardley, S. L. 2022, *ApJL*, 930, L10

Canizares, C. R., Davis, J. E., Dewey, D., et al. 2005, *Publications of the Astronomical Society of the Pacific*, 117, 1144

Caspi, A., McTiernan, J. M., & Warren, H. P. 2014, *ApJL*, 788, L31

Culhane, J. L., Rapley, C., Bentley, R., et al. 1981, *ApJ*, 244, L141

de Vries, C. P., Haas, D., Yamasaki, N. Y., et al. 2018, *JATIS*, 4, 011204

Decaux, V., Beiersdorfer, P., Kahn, S., & Jacobs, V. 1997, *ApJ*, 482, 1076

Del Zanna, G. & Mason, H. E. 2018, *Living Reviews in Solar Physics*, 15, 5

Den Herder, J., Brinkman, A., Kahn, S., et al. 2001, *A&A*, 365, L7

Dere, K., Landi, E., Mason, H., Fossi, B. M., & Young, P. 1997, *A&A* Supplement Series, 125, 149

Dere, K. P., Del Zanna, G., Young, P. R., Landi, E., & Sutherland, R. S. 2019, *ApJ* Supplement Series, 241, 22

Didel, S., Pandey, J. C., & Srivastava, A. 2024, *AJ*, 169, 49

Doschek, G., Feldman, U., & Cowan, R. 1981, *ApJ*, 245, 315

Doschek, G., Kreplin, R., & Feldman, U. 1979, *ApJ*, 233, L157

Doyle, T. F., Holland, M. P., Hill, R. S., et al. 2022, in Space Telescopes and Instrumentation 2022: Ultraviolet to Gamma Ray, Vol. 12181, SPIE, 1495–1506

Drake, J. J., Brickhouse, N. S., Kashyap, V., et al. 2001, *ApJ*, 548, L81

Dufresne, R., Del Zanna, G., Young, P., et al. 2024, *ApJ*, 974, 71

Eckart, M. E., Brown, G. V., Chiao, M. P., et al. 2024, in Space Telescopes and Instrumentation 2024: Ultraviolet to Gamma Ray, Vol. 13093, SPIE, 504–521

Favata, F. & Schmitt, J. H. M. M. 1999, *A&A*, 350, 900

Fekel, F. C. 1983, *ApJ*, 268, 274

Feldman, U., Landi, E., & Doschek, G. 2006, *High Energy Density Physics*, 2, 104

Foster, A., Ji, L., Smith, R., & Brickhouse, N. 2012, *ApJ*, 756, 128

Gabriel, A. 1972, *MNRAS*, 160, 99

Golay, W. W., Mutel, R. L., & Abbuhl, E. E. 2024, *ApJ*, 965, 86

Güdel, M., Audard, M., Smith, K. W., et al. 2002, *ApJ*, 577, 371

Hell, N., Brown, G., Eckart, M., et al. 2025, arXiv preprint arXiv:2506.17106

Hitomi Collaboration, Aharonian, F., Akamatsu, H., et al. 2018, *PASJ*, 70, 12

Huenemoerder, D. P., Phillips, K. J., Sylwester, J., & Sylwester, B. 2013, *ApJ*, 768, 135

Inoue, S., Iwakiri, W. B., Enoto, T., et al. 2024, *ApJL*, 969, L12

Ishisaki, Y., Kelley, R. L., Awaki, H., et al. 2022, in Space Telescopes and Instrumentation 2022: Ultraviolet to Gamma Ray, Vol. 12181, SPIE, 409–430

Ishisaki, Y., Kelley, R. L., Awaki, H., et al. 2025, *JATIS*, 11, 042023

Ishisaki, Y., Yamada, S., Seta, H., et al. 2018, *JATIS*, 4, 011217

Jansen, F., Lumb, D., Altieri, B., et al. 2001, *A&A*, 365, L1

Kaastra, J. & Bleeker, J. 2016, *A&A*, 587, A151

Kaastra, J., Mewe, R., & Nieuwenhuijzen, H. 1996, *UV and X-ray Spectroscopy of Astrophysical and Laboratory Plasmas*, 411

Kaastra, J. S., Raassen, A. J. J., de Plaa, J., & Gu, L. 2024, *SPEX X-ray Spectral Fitting Package*, Zenodo

Katsuda, S., Ohno, M., Mori, K., et al. 2020, *ApJ*, 891, 126

Kelley, R. L., Ishisaki, Y., Costantini, E., et al. submitted, *JATIS*

Kowalski, A. F. 2024, *Living Reviews in Solar Physics*, 21, 1

Kramida, A., Yu, Ralchenko, Reader, J., & and NIST ASD Team. 2024, *NIST Atomic Spectra Database* (ver. 5.12), [Online]. Available: <https://physics.nist.gov/asd> [2025, June 18]. National Institute of Standards and Technology, Gaithersburg, MD.

Kurihara, M., Tsujimoto, M., Audard, M., et al. 2025, *PASJ*, psaf045

Laming, J. M. 2009, *ApJ*, 695, 954

Laming, J. M. 2015, *Living Reviews in Solar Physics*, 12, 1

Laming, J. M. 2021, *ApJ*, 909, 17

Lanzafame, A. C., Brooks, D. H., Lang, J., et al. 2002, *A&A*, 384, 242

Liefke, C., Fuhrmeister, B., & Schmitt, J. H. M. M. 2010, *A&A*, 514, A94

McCammon, D., Moseley, S., Mather, J., & Mushotzky, R. 1984, *Journal of applied physics*, 56, 1263

Midooka, T., Tsujimoto, M., Kitamoto, S., et al. 2021, *JATIS*, 7, 028005

Mochizuki, Y., Tsujimoto, M., Kilbourne, C. A., et al. 2025a, *JATIS*, 11, 042002

Mochizuki, Y., Tsujimoto, M., Leutenegger, M. A., et al. 2025b, *PASJ*, in press

Neupert, W. M. 1968, *ApJ*, 153, L59

Nordon, R. & Behar, E. 2007, *A&A*, 464, 309

Nordon, R. & Behar, E. 2008, *A&A*, 482, 639

Nordon, R., Behar, E., & Güdel, M. 2006, *A&A*, 446, 621

Pandey, J. & Singh, K. 2012, *MNRAS*, 419, 1219

Perdelwitz, V., Navarrete, F., Zamponi, J., et al. 2018, *A&A*, 616, A161

Petit, P., Donati, J.-F., Wade, G., et al. 2004, *MNRAS*, 348, 1175

Phillips, K. 2004, *ApJ*, 605, 921

Phillips, K., Rainnie, J., Harra, L. K., et al. 2004, *A&A*, 416, 765

Porter, F. S., Kilbourne, C. A., Chiao, M., et al. 2024, in Space Telescopes and Instrumentation 2024: Ultraviolet to Gamma Ray, Vol. 13093, SPIE, 444–460

Pottasch, S. R. 1963, *ApJ*, 137, 945

Priest, E. R. & Forbes, T. G. 2002, *A&AR*, 10, 313

Raassen, A., Mewe, R., Audard, M., & Güdel, M. 2003, *A&A*, 411, 509

Rudolph, J. K., Bernitt, S., Epp, S., et al. 2013, *Phys. Rev. Lett.*, 111, 103002

Sawada, M., Cumbee, R., de Vries, C., et al. 2024, in Space Telescopes and Instrumentation 2024: Ultraviolet to Gamma Ray, Vol. 13093, SPIE, 1702–1726

Seli, B., Oláh, K., Kriskovics, L., et al. 2022, *A&A*, 659, A3

Shibata, K. & Magara, T. 2011, *Living Reviews in Solar Physics*, 8, 6

Shipman, R. F., Kitamoto, S., Wolfs, R., et al. 2024, in Space Telescopes and Instrumentation 2024: Ultraviolet to Gamma Ray, Vol. 13093, SPIE, 1617–1626

Smith, R. K., Brickhouse, N. S., Liedahl, D. A., & Raymond, J. C. 2001, *ApJ*, 556, L91

Strassmeier, K., Granzer, T., Weber, M., et al. 2020, *A&A*, 644, A104

Suzuki, H., Kurashima, J., Katsuda, S., et al. submitted, *PASJ*

Tanaka, K., Watanabe, T., Nishi, K., & Akita, K. 1982, *ApJ*, 254, L59

Tashiro, M., Maejima, H., Toda, K., et al. 2020, in Space Telescopes and

Instrumentation 2020: Ultraviolet to Gamma Ray, Vol. 11444, SPIE, 293–303

Telleschi, A., Güdel, M., Briggs, K., et al. 2005, ApJ, 622, 653

Testa, P. 2010, Space Sci. Rev., 157, 37

To, A. S., Brooks, D. H., Imada, S., et al. 2024, A&A, 691, A95

Tsuboi, Y., Yamazaki, K., Sugawara, Y., et al. 2016, PASJ, 68, 90

Van den Besselaar, E. J., Raassen, A., Mewe, R., et al. 2003, A&A, 411, 587

Warren, H. P. 2005, ApJS, 157, 147

Warren, H. P. 2014, ApJL, 786, L2

Watanabe, T. 2024, ApJ, 965, 41

Weisskopf, M. C., Tananbaum, H. D., Van Speybroeck, L. P., & O'Dell, S. L. 2000, X-ray optics, instruments, and missions iii, 4012, 2

Wilms, J., Allen, A., & McCray, R. 2000, ApJ, 542, 914